Journal of Solid State Chemistry 316 (2022) 123640

Contents lists available at ScienceDirect

Journal of Solid State Chemistry

journal homepage: www.elsevier.com/locate/jssc

Modulating interfacial defects for dual-enhancing chromaticity and stability of cerium sulfide

Xuan Sun [a,b], Wei Dong [c], Chenjie Lou [b], Shuqin Chang [b], Ruiping Deng [c], Ran Pang [c], Guangcan Bai [d], Guoquan Liu [d], Jipeng Fu [a,*], Mingxue Tang [b,**], Shiqing Xu [a], Chengyu Li [c], Hongjie Zhang [c]

HPSTAR 1548-2022

[a] Key Laboratory of Rare Earth Optoelectronic Materials and Devices of Zhejiang Province, Institute of Optoelectronic Materials and Devices, China Jiliang University, Hangzhou, 310018, China
[b] Center for High Pressure Science and Technology Advanced Research, Beijing, 100094, China
[c] Changchun Institute of Applied Chemistry, Chinese Academy of Sciences, Jilin Province, 130022, ChangChun, China
[d] State Key Laboratory of Natural and Biomimetic Drugs, School of Pharmaceutical Sciences, Peking University, 100191, Beijing, China
[e] College of Materials Science and Engineering, Tianjin University, 300072, Tianjin, China

ARTICLE INFO

Keywords:
Cerium sulfides
Defect modulation
Interfacial correlation
Chromaticity
Stability

ABSTRACT

To obtain rare earth sulfides with satisfied chromaticity and stability for diverse applications in the field of pigment, a harnessed synthetic molecular strategy for *in-situ* growth of $CePO_4$ as an interlayer between core Ce_2S_3 substrate and the outer SiO_2 layer is proposed. High-angle annular dark-field scanning transmission electron microscope (HAADF-STEM), electron paramagnetic resonance (EPR), and Raman analysis reveal that the transition layer $CePO_4$ significantly reduces the lattice spacing differences and reduces the oxygen activity on the interface, resulting in excellent chromaticity ($L^* = 51.9$, $a^* = 45.0$, $b^* = 30.0$) and stability for γ-Ce_2S_3@$CePO_4$@SiO_2. These insights will advance the fundamental knowledge of core-shell crystal engineering and enable new ways to promote the application of rare earth sulfides.

1. Introduction

Inorganic pigments have attracted intensive attention from both academic research and potential industrial application because of their competitive stability properties. However, the compounds of red inorganic pigments were usually made of toxic transition metal, such as cadmium selenide, cadmium sulphoselenides, and palladium chromate, which would release toxic ions under acid-base environment and photothermal effect, further threatening human health and the natural environment [1–5]. Alternatively, γ-Ce_2S_3, one of rare earth sulfides, could potentially serve as a coloring pigment owing to its favorable brightness and non-toxicity properties. However, the presence of vacancies on the cationic sublattice and the oxophilic nature of Ce^{3+} in γ-Ce_2S_3 result in its poor stability, being limited from wide application, especially when the temperature exceeds 300 °C [6].

To improve the stability of pristine γ-Ce_2S_3, the strategy of construction of core-shell chemical architecture was employed to prevent or weaken γ-Ce_2S_3 oxidation at high temperature [7–9]. For instance, an outer ZnO layer was introduced to improve the stability of γ-Ce_2S_3 at high temperature. The stability has been improved by the aid of the ZnO layer with the decreasing in chromaticity properties [2]. Similarly, the highly condensed c-SiO_2 was coated onto γ-Ce_2S_3 pigments to effectively protect γ-Ce_2S_3 from oxidation at raised temperatures up to 883 °C, while a^* values decreased [10]. In short, the improved stability at the expense of chromaticity was still failed to meet the application standard, and the further research for achieving both enhanced stability and chromaticity were urgently needed. Meanwhile, very limited information is available on the precise nature of the core-shell interface and the way influencing the spectra. The possible lattice defects or spacing mismatching at the interface may creative between the active core and the coating layer, which would cause potential spectral energy loss and further result in negative impact on chromaticity [3]. Therefore, in-depth understanding of the effect of the interface on the performance and the development of an appropriate synthetic strategy was vitally in demand.

In this work, a modulating layer $CePO_4$ was introduced between the core γ-Ce_2S_3 and the coating SiO_2 layer to reduce the lattice spacing

* Corresponding author.
** Corresponding author.
E-mail addresses: fujipeng@cjlu.edu.cn (J. Fu), mingxue.tang@hpstar.ac.cn (M. Tang).

https://doi.org/10.1016/j.jssc.2022.123640
Received 6 August 2022; Received in revised form 20 September 2022; Accepted 30 September 2022
Available online 5 October 2022

mismatch and the defects, aiming at improving both stability and chromaticity of γ-Ce_2S_3. The performances of bilayer-shelled γ-Ce_2S_3@$CePO_4$@SiO_2 were fully characterized, and the outstanding advantages were demonstrated compared with that of single-layer coated structure and pristine. High resolution TEM and electron paramagnetic resonance (EPR) were employed to probe the local defects and interfacial structures from an atomic-scale perspective. The structure-activity mechanism related to double coating structure provides an efficient strategy for interfacial modulation, which is crucial for applications of rare earth sulfides.

2. Experimental

2.1. Preparation of γ-Ce_2S_3

All precursors are AR pure supplied by Macklin (Shanghai, China). Typically, the mixture of $Ce_2(CO_3)_3{\cdot}xH_2O$, Na_2CO_3, and AlF_3 with a molar ratio of 20:0.3:0.7 was fully grounded in an agate mortar and prepared by using solid-state reaction [11]. Excess sulfur powder (molar ratio of Ce:S = 1:4) with the obtained mixture was added into a cylindrical crucible with carbon particles on the bottom layer. Then, the power was placed in a furnace calcined at 950 °C for 2 h, followed by ball milling for an hour to obtain the γ-Ce_2S_3.

2.2. Preparation of γ-Ce_2S_3@SiO_2

0.02 g Polyvinyl pyrrolidone (PVP), 2 mL of ammonia water, and γ-Ce_2S_3 were successively mixed in the 40 mL anhydrous ethanol. Meanwhile, 0.4 mL ethyl orthosilicate was added and stirred for 2 h at room temperature. Then, they were filtered and washed with deionized water and ethanol several times before drying at 120 °C.

2.3. Preparation of γ-Ce_2S_3@$CePO_4$

γ-Ce_2S_3, $Zn(H_2PO_4)_2$, sodium citrate with a certain molar ratio of 300: 16: 5 were added in the 50 mL deionized water and stirred for 2 h at room temperature. The products were washed with distilled water and ethanol several times with proper drying afterwards.

2.4. Preparation of γ-Ce_2S_3@$CePO_4$@SiO_2

The γ-Ce_2S_3@$CePO_4$ was dispersed in the 40 mL anhydrous ethanol. 0.02 g polyvinyl pyrrolidone (PVP) and 2 mL of ammonia water were added successively. Meanwhile, 0.4 mL ethyl orthosilicate was added and stirred for 2 h. Then, the as-prepared sample was obtained by filtration, washed with deionized water and ethanol several times, followed by drying at 120 °C.

2.5. Characterizations

X-ray diffraction (XRD) data for all samples were collected from a diffractometer (D2 PHASER, Bruker, Germany) with Cu Kα radiation source (30 kV, 10 mA, λ = 0.15418 nm) which were scanned from 10° to 70° at a scanning rate of 10°/min. The qualitative analysis of the microstructure and elements of the sample was analyzed by scanning electron microscope (SEM) with an acceleration voltage of 10 kV (SU8010, Hitachi, Japan). The samples were characterized by Fourier infrared spectrometer (NicoletiS50, Thermo Fisher Scientific, American) in the range of 400–2000 cm^{-1} at a scanning rate of 0.153 cm/s. High Angle Annular Dark Field Scanning Transmission Electron Microscopy (HAADF-STEM) and mapping were performed on a double monochromator and probe/image (Titan Themis 60-300 S/TEM, Thermo Fisher Scientific, American) equipped with an Energy Dispersive Spectrometer (EDS). Electron paramagnetic resonance (EPR) spectra were acquired from a spectrometer (JES-FA200, JEOL, Japan) at room temperature with modulation frequency 100 kHz. Diffuse reflectance spectrum was recorded on ultraviolet–visible–near-infrared spectrophotometer (UV-3600, Shimadzu, Japan), the sample was measured with a high-resolution 0.1 nm integrating sphere device and referenced to $BaSO_4$ for calibration from 400 nm to 700 nm at a speed of 1 nm/s. DSC experiments were conducted on a differential thermal analyzer (DTA 404 PC, Netzsch, Germany). The samples (10 mg) were heated from 30 °C to 700 °C at a heating rate of 10 °C min^{-1} under the air atmosphere. Chemical composition and elemental states were detected by X-ray photoelectron spectrometer (ESCALAB 250, Thermo Scientific, USA) equipped with Al Ka radiation monochromatic source. Ramam spectra of samples were collected in the range of 200–800 cm^{-1} using a Ramam spectrometer (InVia-Reflex, Renishaw, UK) with an excitation wavelength of 785 nm and resolution of 1 cm^{-1} at 100 mW laser power. Solid state nuclear magnetic resonance (NMR) measurements were performed on a Bruker 400 MHz spectrometer (AVANCE NEO, Bruker, Germany). The study materials were filled into 3.2 mm rotors and spun at a magic angle spinning (MAS) rate 14 kHz. Single pulse was used to polarize and record the signals.

3. Result and discussion

The fabrication process of γ-Ce_2S_3, γ-Ce_2S_3@SiO_2, γ-Ce_2S_3@$CePO_4$, γ-Ce_2S_3@$CePO_4$@SiO_2 are demonstrated in Scheme 1, and their crystal structures were characterized by XRD as shown in Fig. 1a. The XRD peaks of γ-Ce_2S_3 match well with the standard card PDF#75–1948 in cubic Th_3P_4 phase. After coating with the SiO_2 layer, the cubic phase was maintained for γ-Ce_2S_3@SiO_2. The amorphous nature of SiO_2, which was also confirmed by ^{29}Si NMR spectrum as shown in Fig. S1. The existence of $CePO_4$ was confirmed by extra small peaks appearing at 31.12°, 37.35°, and 52.68° for both γ-Ce_2S_3@$CePO_4$ and γ-Ce_2S_3@$CePO_4$@SiO_2. Small peaks at about 25.5° and 31.7° are observed for the Al_2O_3 impurity originated from the conversion of excess Al doping [12,13]. As shown in Fig. 1b, the γ-Ce_2S_3@$CePO_4$@SiO_2 contains P, Si, Ce, S, O, and C elements, where the S 2p signal was detected at 155.4 eV, and the peak near 133.8 eV is associated with SiO_2. In addition, the small peak near 133.8 eV that is associated with PO_4^{3-}. The C element of the referencing spectra at the binding energy of 284.6 eV was detected. The O 1s peak at 532.7 is contributed to the active surface oxygen (OH^-). Interestingly, compared with other γ-Ce_2S_3-based composite materials, the O 1s peaks of γ-Ce_2S_3@$CePO_4$@SiO_2 shift to the higher binding energy as shown in Fig. S2a, indicating the generation of reactive oxygen species could be suppressed [14]. Similarly, compared with γ-Ce_2S_3@$CePO_4$, the P 2p peak is observed that shows positive shift in the binding energy of γ-Ce_2S_3@$CePO_4$@SiO_2 (Fig. S2b), because the interaction of the SiO_2 and $CePO_4$ interface promotes the movement of electrons, reducing the surface oxygen activity [15–17]. Furthermore, the Ce 3d signals of γ-Ce_2S_3 and γ-Ce_2S_3@$CePO_4$@SiO_2 were plotted in Fig. 1c. There are two characteristic peaks at 885.1 eV and 904.2 eV for Ce $3d_{5/2}$ and Ce $3d_{3/2}$ respectively, indicating the Ce in the γ-Ce_2S_3@$CePO_4$@SiO_2 still presents trivalent Ce^{3+} [18].

The morphology of γ-Ce_2S_3 and γ-Ce_2S_3 composite materials are shown in Fig. S3 by scanning electron microscopy (SEM). The particle diameter of the pristine γ-Ce_2S_3 is approximately 0.5–1.5 μm with irregular configuration and particle aggregation. After being coated with $CePO_4$ and/or SiO_2 shell, the particles with single shell show diameter of 1–3 μm, and the size of bilayer-shelled particles is 1.5–5 μm with good dispersion.

The composite structures were further verified by energy dispersive X-ray spectroscopy (EDS). As shown in Fig. 2a, SiO_2 layer is about 4 nm in thickness, and the intermediate $CePO_4$ layer is in the range of 10–20 nm, which are coated on the core γ-Ce_2S_3 that is observed as the dark and dense region. Ce, P, S, and Si elements are detected and distributed homogenously, which corresponding to SiO_2 layer (Green) and interlayer $CePO_4$ (Red) respectively from the sum of EDS maps (right-top image in Fig. 2a). The EDS elemental mappings of other γ-Ce_2S_3 composite materials are also supplied in Figs. S4–S6 for reference.

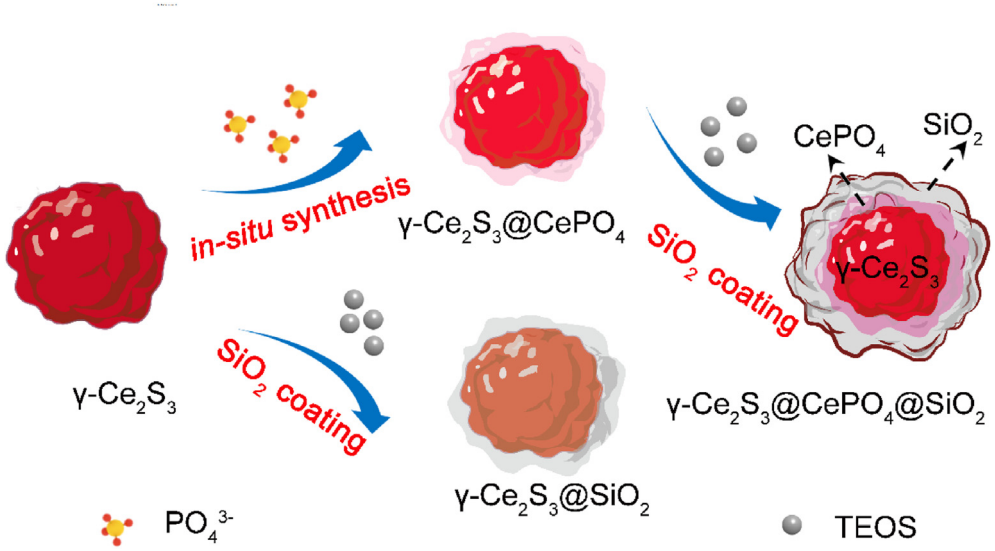

Scheme 1. Preparation process of γ-Ce_2S_3@SiO_2, γ-Ce_2S_3@$CePO_4$ and γ-Ce_2S_3@$CePO_4$@SiO_2. TEOS stands for tetraethoxysilane.

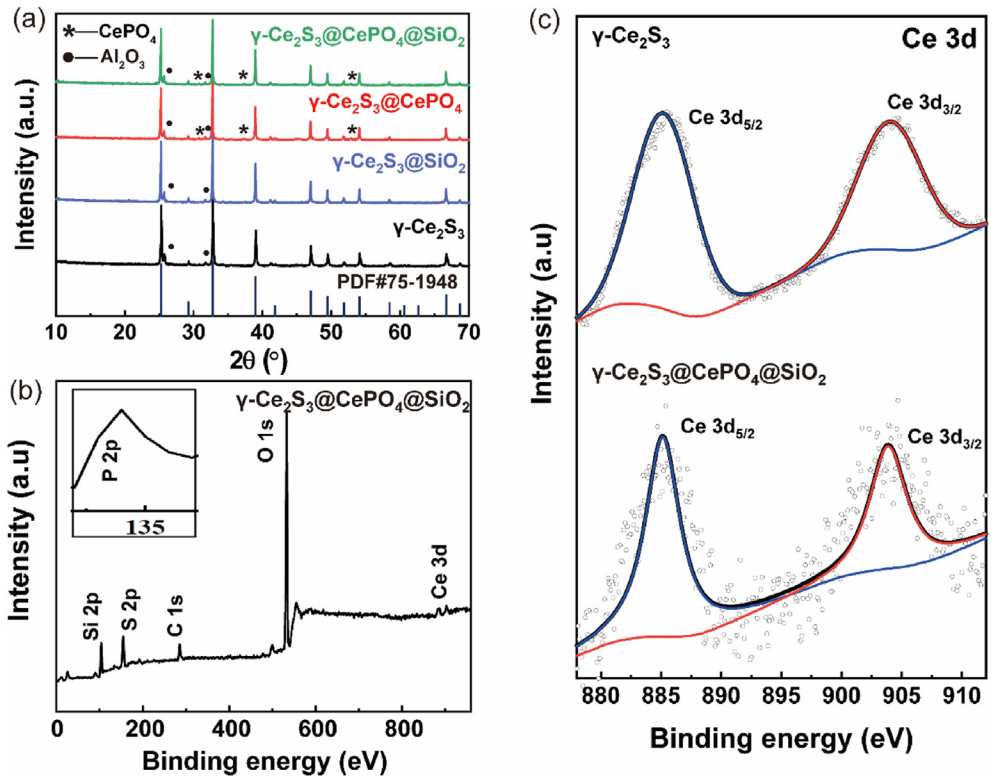

Fig. 1. (a) XRD patterns of γ-Ce_2S_3, γ-Ce_2S_3@SiO_2, γ-Ce_2S_3@$CePO_4$, γ-Ce_2S_3@$CePO_4$@SiO_2. (b) Full survey XPS spectrum of γ-Ce_2S_3@$CePO_4$@SiO_2. (c) XPS spectra of Ce 3d in γ-Ce_2S_3 and γ-Ce_2S_3@$CePO_4$@SiO_2.

In Fig. 2b, it is observed Raman peaks at 403 cm^{-1} and 455 cm^{-1} are characteristic of γ-Ce_2S_3 [19]. As coated with SiO_2/$CePO_4$, the broad Raman band at 403 cm^{-1} gradually disappeared. A huge enhancement in the main peak intensity with the increasing coating thickness, which is consistent with a gradual increase in Si–O, δs (P–O) bond concentration during the coating layer growth. The Raman peaks of all samples are overlapped in the range of 400–500 cm^{-1}, which are divided into different peaks as shown in Fig. S7. The vibration peaks of Si–O chemical keys have a low wide Raman Peak around at 440 cm^{-1} where the band appearing at near 400-460 cm^{-1} are assigned to δs (P–O) symmetrical bending mode [20,21]. The assignments of PO_4^{3-} band in $CePO_4$ are complicated due to different structural state and chemical composition. For γ-Ce_2S_3@$CePO_4$@SiO_2, the different shell materials were confirmed by fitting functions ascribed to 440, 455, and 465 cm^1 for the vibration of Si–O, Ce–S and δs (P–O) bonds, respectively (Fig. S7c). Significantly, the full width at half maximum (FWHM) of Raman peaks slightly decreases from 26.92 cm^{-1} (γ-Ce_2S_3@SiO_2) to 22.26 cm^{-1} (γ-Ce_2S_3@$CePO_4$@-SiO_2) (Fig. 2b), reflecting the decreasing of defects by introducing the intermediate $CePO_4$ layer [22]. For all samples, the EPR spectra show resonance signals at g = 2.0003, corresponding to the presence of unpaired or delocalized electrons from sulfur vacancies (V_s) or defects (Fig. 2c) [23,24]. Compared with γ-Ce_2S_3@SiO_2, the γ-Ce_2S_3@$CePO_4$

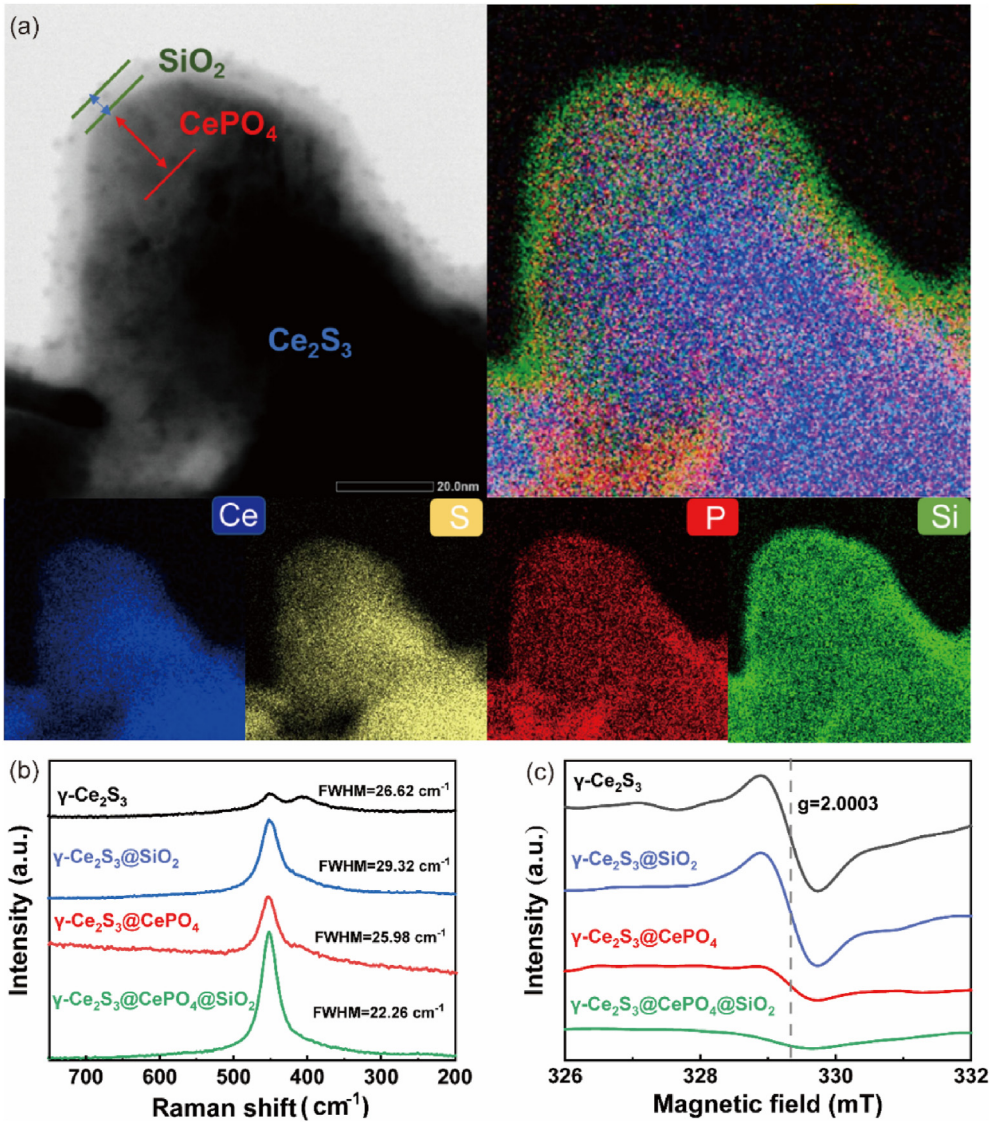

Fig. 2. (a) EDS-mapping images of γ-Ce_2S_3@$CePO_4$@SiO_2, (b) Raman spectra of γ-Ce_2S_3 and γ-Ce_2S_3 composite materials. (c) EPR spectra of γ-Ce_2S_3, γ-Ce_2S_3@SiO_2, γ-Ce_2S_3@$CePO_4$, and γ-Ce_2S_3@$CePO_4$@SiO_2 obtained at room temperature.

sample shows relative broader and weaker signal, because the $CePO_4$ layer has better interface contact with core material through *in-situ* growth, suggesting lower lattice spacing differences for γ-Ce_2S_3@$CePO_4$@SiO_2 [25,26].

In order to gain deep insights into microstructures, the atomic scale and the crystal lattice were detected by aberration-corrected high-angle annular dark-field scanning TEM (HAADF-STEM) (Fig. 3). The STEM images of γ-Ce_2S_3, γ-Ce_2S_3@SiO_2, γ-Ce_2S_3@$CePO_4$ and γ-Ce_2S_3@$CePO_4$@SiO_2 were respectively shown in Fig. 3a–d. The STEM image (Fig. 3e) and Fast Fourier Transformation (FFT) of γ-Ce_2S_3 (Fig. 3j-l) show clear lattice fringes for the inner part of γ-Ce_2S_3 with the (211) and (310) planes from the [1–31]-zone axis, and the edges of γ-Ce_2S_3 are amorphous (Fig. 3l). For γ-Ce_2S_3@SiO_2, the enlarged interface of γ-Ce_2S_3@SiO_2 (Fig. 3m) and the electron diffraction patterns (Fig. 3n–p), from which the shell material (SiO_2) and the core section (γ-Ce_2S_3) were well assigned to amorphous and crystalline planes (400) and (211) respectively. For γ-Ce_2S_3@$CePO_4$, the electron diffraction deriving from the STEM images also confirmed that the (211) and (321) planes were from the core γ-Ce_2S_3 phase, and the (310) and (110) planes were from the out-layer $CePO_4$ (Fig. 3r–t). In addition, the growth of $CePO_4$ shell with well lattice matching is shown in Fig. 3q. However, the STEM image of interface between γ-Ce_2S_3 layer and SiO_2 layer shows lattice disorder (Fig. 3m). Taking the advantage of well-formed interface of γ-Ce_2S_3 and $CePO_4$, the intermediate layer ($CePO_4$) between the γ-Ce_2S_3 core and the outer shell SiO_2 was inserted to serve as a "lattice adapter" for improving interface compatibility or avoiding defects caused by interface interaction [3,27,28]. As shown in Fig. 3v-x, the FFT pattern of $CePO_4$ in γ-Ce_2S_3@$CePO_4$@SiO_2 area is assigned to (100) and (101) planes that parallels to the [0–1 0]-zone axis, and the amorphous of SiO_2 was revealed by the electron diffraction pattern, confirming the result from XRD pattern of γ-Ce_2S_3@$CePO_4$@SiO_2 (Fig. 1a).

The chromaticity and thermal stability of the aforementioned materials were performed and analyzed. As shown in Fig. 4a, there is prominent absorption in the range of 400–550 nm for all γ-Ce_2S_3 composite materials. The intensity of reflection spectra of γ-Ce_2S_3 coated with SiO_2 show lower reflectance than that of pristine γ-Ce_2S_3 from 590 to 700 nm. The reflectance decreases of the γ-Ce_2S_3@SiO_2 is caused by the energy loss of light wave due to the interaction with surfaces of γ-Ce_2S_3 and SiO_2. On the contrary, the diffuse reflectance of γ-Ce_2S_3@$CePO_4$ and γ-Ce_2S_3@$CePO_4$@SiO_2 are enhanced about 10% to reach ~80% because of the polishing effect of the zinc dihydrogen phosphate on the irregular surface of γ-Ce_2S_3 and the following formed $CePO_4$ layer *in-situ*. The

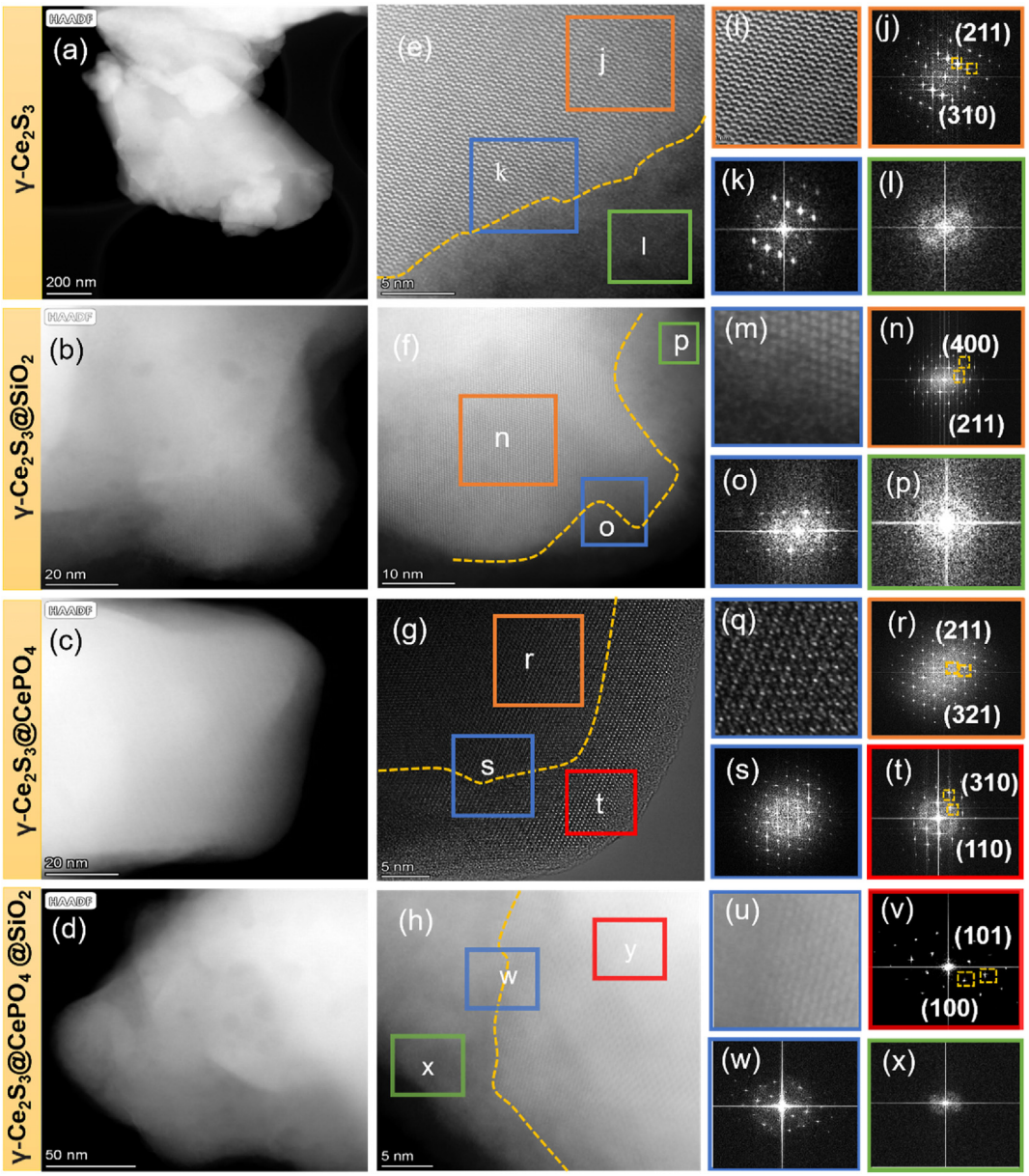

Fig. 3. (a–d) HADDF-STEM images of γ-Ce_2S_3 composite materials, (e–h) Magnified STEM images taken from the edges of samples in (a–d), (i) Magnified STEM image taken from the corresponding square area in (e), (j–l) Electron diffraction patterns taken from the corresponding γ-Ce_2S_3 (orange box), the grain boundary (blue box), shell (green box) square area in (e), (m) Magnified STEM image taken from the corresponding square area in (f), (n–p) Electron diffraction patterns taken from the corresponding core (orange box), core-shell interface (blue box), shell (green box) square area in (f), (q) Magnified STEM image taken from the corresponding square area in (s), (r–t) Electron diffraction pattern taken from the corresponding core (orange box), core-shell interface (blue box), shell (red box) square area in (g), (h) Magnified STEM image taken from the corresponding square area with the thickness of SiO_2, (u) Magnified STEM image taken from the corresponding square area in (h). (v–x) Electron diffraction pattern taken from the corresponding core (red box), core-shell interface (blue box), shell (green box) square area in (h).

reflectivity of γ-Ce_2S_3@$CePO_4$ is improved, which reaches the maximum in the range of 590–700 nm, suggesting the highest lightness value. However, it shows the lowest absorption in the range of 400–500 nm. Furthermore, the diffuse reflectance of γ-Ce_2S_3@$CePO_4$ shows approximately same spectral shape and intensity of in the region of 590–700 nm, accompanied by the strong absorption band between 400 and 550 nm. In addition, the absolute differences values ($\Delta R_{(400\text{-}700)}$) between the maximum reflectance (at 700 nm) and minimum absorption (at 400 nm) for the four materials are summarized in Table S1, from which the largest value is found for γ-Ce_2S_3@$CePO_4$@SiO_2.

In order to visually measure the color properties of human eyes to the light, the CIE chromaticity value a^* and value b^* were calculated by 1931 CIE-*XYZ* color system. The tristimulus values of the quasi-observer derive from the CIE standard illuminator with the light source C and the field angle of 2° ($X_0 = 98.07$, $Y_0 = 100.00$, $Z_0 = 118.22$). According to CIE 1931 $L^*a^*b^*$, where L^* represents the lightness of the color, a^* represents the red-green axis of the space, and b^* represents the blue-yellow axis of the space [29]. The chroma values of the sample were calculated by the following formulas:

$$L^* = 116\left[f\left(\frac{Y}{Y0}\right) - \frac{16}{116}\right] \quad (1)$$

$$a^* = 500\left[f\left(\frac{X}{X0}\right) - f\left(\frac{Y}{Y0}\right)\right] \quad (2)$$

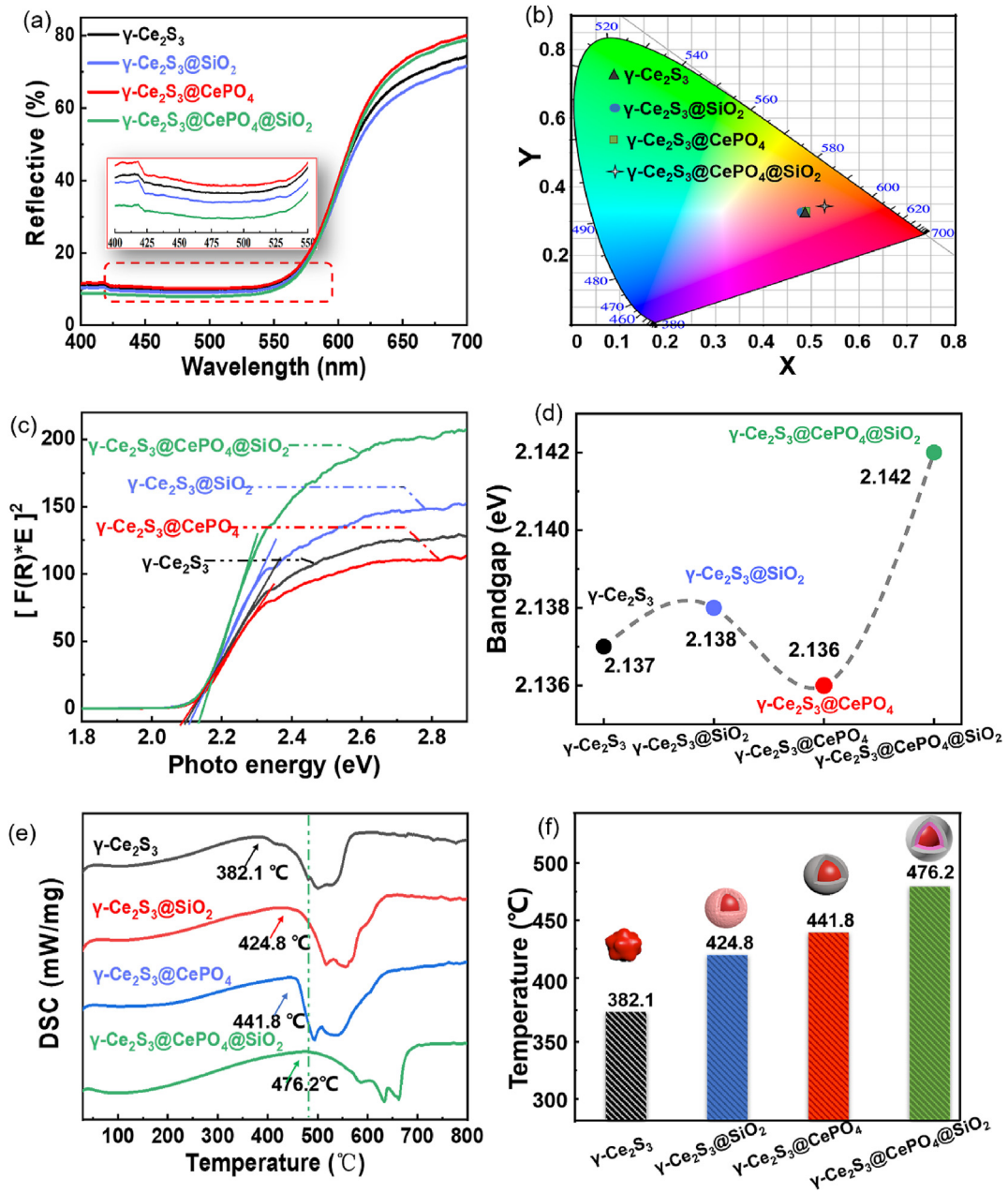

Fig. 4. (a) Visible light reflectance spectra and (b) CIE mapping of γ-Ce_2S_3-based composite materials. (c–d) Optical band gap determined from the visible diffuse reflectance spectra. (e–f) DSC curves and oxidation temperatures for γ-Ce_2S_3-based composite materials.

$$b^* = 200\left[f\left(\frac{Y}{Y0}\right) - f\left(\frac{Z}{Z0}\right)\right] \tag{3}$$

$$f(w) = \begin{cases} W^{\frac{1}{3}}, W \geq \left(\frac{24}{116}\right)^3 \\ 7.787 + \frac{16}{116}, W \leq \left(\frac{24}{116}\right)^3 \end{cases} \tag{4}$$

The calculated results of CIE $L^*a^*b^*$ values are summarized in Table 1. The lightness parameters L^* increases from 53.11 to 54.05 for the pristine γ-Ce_2S_3 to the γ-Ce_2S_3@$CePO_4$, being consistent with the maximum reflection in the long wavelength range. While both γ-Ce_2S_3@SiO_2 and γ-Ce_2S_3@$CePO_4$@SiO_2 of parameters L^* decrease slightly, suggesting the SiO_2 layer has a negative influence on the lightness. Meanwhile, except for γ-Ce_2S_3@SiO_2, the major improvement is found for both a^* and b^* parameters for other γ-Ce_2S_3-based composite

Table 1
Colorimetric values of γ-Ce_2S_3-based composite materials.

Sample	L^*	a^*	b^*	Photo
γ-Ce_2S_3	53.11	41.00	26.00	
γ-Ce_2S_3@SiO_2	51.70	40.40	25.78	
γ-Ce_2S_3@$CePO_4$	54.05	42.68	26.18	
γ-Ce_2S_3@$CePO_4$@SiO_2	51.90	45.00	30.00	

materials. Especially for γ-Ce_2S_3@$CePO_4$@SiO_2, the parameters of a^* and b^* increase from (41.00, 26.00) to (45.00, 30.00), corresponding to the CIE chromaticity coordinates ranged from (0.505, 0.340) to (0.527, 0.341) in Fig. 4b.

The correlation between band gap and absorption coefficient is $[F(R)h\nu]^2 = C_1(h\nu\text{-}E_g)$, where $F(R)$ is the *Kubella-Munk* function, in which $F(R) = (1\text{-}R^2)/2R$, and R is defined as the reflectivity of sample's spectral reflectance; C_1 is the proportional constant; the $h\nu$ photon energy is taken as the abscissa and the $[F(R)h\nu]^2$ as the ordinate; and the intersection of the tangent and the x-axis is then the band gap width Eg Refs. [30–32]. As shown in Fig. 4c-d, the band gaps of all samples were calculated as in the range of 2.136–2.142 eV, which are consistent with the results from the CIE color coordinates. In detail, band gaps of 2.137, 2.138, and 2.136 eV are determined for γ-Ce_2S_3, γ-Ce_2S_3@SiO_2, and γ-Ce_2S_3@$CePO_4$, respectively. However, a large deviation, 2.142 eV, is detected in γ-Ce_2S_3@$CePO_4$@SiO_2. According to the band gap engineering of semiconductor nanocrystals, band gap shifts are related to the defects at the sample surface and interfacial lattice space differences, which can be regulated through surface reconstruction and passivation effects for core-shell structure [28,33]. We speculate that the wider band gap for γ-Ce_2S_3@$CePO_4$@SiO_2 is attributed to the modification of the surface defects by the intermediate adapted $CePO_4$ layer as an effective barrier to inhibit the recombination of electrons and holes, leading to the wider range of chromaticity. On the contrary, γ-Ce_2S_3@$CePO_4$ presents the smallest band gap, reflecting that electron-hole pair is easier to recombine. As shown in Fig. 4a (the magnified red dashed region), γ-Ce_2S_3@$CePO_4$ has the lowest absorption in the visible short-wave region, although it has the strongest reflectivity in the long-wave region, resulting in chromaticity a^* and b^* values second only to that of γ-Ce_2S_3@$CePO_4$@SiO_2.

The thermal stability is evaluated by differential scanning calorimetry (DSC). As shown in Fig. 4e and f, the γ-Ce_2S_3 is easily oxidized at 300–400 °C, and the exothermic peak can be further enhanced to 424.8 °C and 441.8 °C for γ-Ce_2S_3 coated with SiO_2 and $CePO_4$, respectively. It is worth noting that the inserted $CePO_4$ layer significantly improves the thermal stability (Fig. 4f), and oxidation temperature of γ-Ce_2S_3@$CePO_4$@SiO_2 reaches up to 476 °C. The acid stability was tested with acetic acid (pH = 4) for all samples (0.3 g) as shown in Fig. S8. With the increase of acid corrosion time, the color change of γ-Ce_2S_3 and γ-Ce_2S_3@SiO_2 from red to brown in 30 min was observed; γ-Ce_2S_3@$CePO_4$ shows slightly change; However, no further color change was observed for γ-Ce_2S_3@$CePO_4$@SiO_2 even after 2 h. In a word, $CePO_4$ as an interlayer modulated core material γ-Ce_2S_3, which is beneficial to improve both thermal and acid stability.

4. Conclusions

In summary, the pristine γ-Ce_2S_3 was obtained by the solid state reaction and an adapt $CePO_4$ interlayer was successfully introduced onto cerium sulfide. The superior spectral and stability properties were achieved by forming the double-layered core-shell composite as γ-Ce_2S_3@$CePO_4$@SiO_2. The new-structure interactions and relevant mechanisms were revealed by high resolution HAADF, short-range magnetic resonance and Raman. The intermediate $CePO_4$ layer reduced not only the differences of lattice spacing, but also the defects between Ce_2S_3 and SiO_2, further resulting in enhanced lightness (L^*), red chromaticity (a^*) and stability. The structure-activity relationship and superior performances of γ-Ce_2S_3@$CePO_4$@SiO_2 provide a prospect for the development of the rare earth sulfide composite material.

CRediT authorship contribution statement

Xuan Sun: Investigation, Data analysis, and Writing of the original draft. **Wei Dong:** Design of experiments. **Chenjie Lou, Shuqin Chang:** Writing of the editing. **Ruiping Deng, Ran Pang, Guangcan Bai, Guoquan Liu, and Huilin Hu:** conducting experiments. **Jipeng Fu and Mingxue Tang:** Funding acquisition, Writing - review & editing, Supervision. **Shiqing Xu, Chengyu Li and Hongjie Zhang:** Funding acquisition.

Declaration of competing interest

The authors declare that they have no known competing financial interests or personal relationships that could have appeared to influence the work reported in this paper.

Data availability

Data will be made available on request.

Acknowledgment

This work is financially supported by the Natural Science Foundation of Zhejiang Province (Grant No. LQ21E020006), the Fundamental Research Funds for the Provincial Universities of Zhejiang (Grant No. 2021YW46), and acknowledge the support from the National Natural Science Foundation of China (No. 62205322).

Appendix A. Supplementary data

Supplementary data to this article can be found online at https://doi.org/10.1016/j.jssc.2022.123640.

References

[1] M. Jansen, H.P. Letschert, Inorganic yellow-red pigments without toxic metals, Nature 404 (2000) 980–982.
[2] W.X. Mao, W. Zhang, Z.X. Chi, R.W. Lu, A.M. Cao, L.J. Wan, Core–shell structured Ce_2S_3@ZnO and its potential as a pigment, J. Mater. Chem. A. 3 (2) (2015) 176–2180.
[3] P. Reiss, M. Protière, L. Li, Core/shell semiconductor nanocrystals, Small 5 (2009) 154–168.
[4] D. Rangppa, T. Naka, A. Kondo, M. Ishii, T. Kobayashi, T. Adschiri, Transparent $CoAl_2O_4$ hybrid nano pigment by organic ligand-assisted supercritical water, J. Am. Chem. Soc. 129 (2007) 11061–11066.
[5] Guang Yang, Hao Ding, Daimei Chen, Weihua Ao, Jian Wang, Xifeng Hou, A simple route to synthesize mesoporous titania from $TiOSO_4$: influence of the synthesis conditions on the structural, pigments and photocatalytic properties, Appl. Surf. Sci. 376 (2016) 227–235.
[6] X. Li, Y. Li, Z. Wang, Y. Hong, Z. Li, Influence of Ba^{2+}doping on the properties and thermal stability of γ-Ce_2S_3, Appl. Phys. 125 (518) (2019).
[7] Y. Ding, J. Gu, T. Zhang, A.X. Yin, L. Yang, Y.W. Zhang, C.H. Yan, Chemoaffinity-mediated synthesis of $NaRES_2$ -based nanocrystals as versatile nano-building blocks and durable nano-pigments, J. Am. Chem. Soc. 134 (2012) 3255–3264.
[8] Y. Huang, Z. Guo, H. Liu, S. Zhang, P. Wang, J. Lu, Y. Tong, Heterojunction architecture of N-doped WO_3 nanobundles with Ce_2S_3 nanodots hybridized on a carbon textile enables a highly efficient flexible photocatalyst, Adv. Funct. Mater. 29 (2019), 1903490.
[9] B. Liu, X. Hu, X. Li, Y. Li, C. Chen, K. Lam, Preparation of ZnS@In_2S_3 Core@shell composite for enhanced photocatalytic degradation of gaseous O-dichlorobenzene under visible light, Sci. Rep. 7 (2017), 16396.
[10] Y. Li, S. Le, Z. Wang, Y. Hong, K. Li, Q. Pu, Preparation and characterization of the Sr^{2+}-doped γ-Ce_2S_3@c-SiO_2 red pigments exhibiting improved temperature and acid stability, Appl. Surf. Sci. 508 (2020), 145266.
[11] K. Hui, W. Dong, J. Fu, M. Tang, Q. Wei, C. Li, H. Zhang, Dual-enhancement of chromaticity and thermal stability: in-situ synthesis of core–shell γ-Ce_2S_3@$CePO_4$ configuration, J. Rare Earths. 40 (2022), 800-806.
[12] Y. Li, Y. Gao, Z. Wang, Z. Shen, Y. Hong, F. Song, Synthesis and characterization of aluminum-based γ-Ce_2S_3 composite red pigments by microemulsion method, J. Alloys Compd. 812 (2020), 152100.
[13] J. Xiang, P. Li, Y. Song, X. Liu, H. Chong, S. Jin, Y. Pei, X. Yuan, M. Zhu, X-ray crystal structure, and optical and electrochemical properties of the $Au_{15}Ag_3(SC_6H_{11})_{14}$ nanocluster with a core–shell structure, Nanoscale 7 (2015) 18278–18283.
[14] C. Zhang, R. Lu, C. L, L. Yuan, J. Wang, Y. Zhao, C. Yu, High yield electrosynthesis of hydrogen peroxide from water using electrospun $CaSnO_3$@Carbon fiber membrane catalysts with abundant oxygen vacancy, Adv. Funct. Mater. 31 (2021), 2100099.
[15] G. Greczynski, L. Hultman, The same chemical state of carbon gives rise to two peaks in X-ray photoelectron spectroscopy, Sci. Rep. 11 (2021), 11195.
[16] P. Zhang, L. Li, D. Nordlund, H. Chen, L. Fan, B. Zhang, X. Sheng, Q. Daniel, L. Sun, Dendritic core-shell nickel-iron-copper metal/metal oxide electrode for efficient electrocatalytic water oxidation, Nat. Commun. 9 (2018) 381.

[17] X.-B. Dong, X. Zhang, X. Yu, Z. Jiang, X. Li, C. Li, Z. Sun, S. Zheng, D. Dionysiou, A novel rutile TiO_2/$AlPO_4$ core-shell pigment with substantially suppressed photoactivity and enhanced dispersion stability, Powder Technol. 366 (2020), 537–545.
[18] E. Bêche, P. Charvin, D. Perarnau, St Abanades, G. Flamant, Ce 3d XPS investigation of cerium oxides andmixed cerium oxide ($Ce_xTi_yO_z$), Surf. Interface Anal. 40 (2008) 264–267.
[19] I. Vasilyeva, B. Ayupov, A. Vlasov, V. Malakhov, P. Maestro, Color and chemical heterogeneities of γ-[Na]-Ce_2S_3 solid solutions, J. Alloys Compd. 268 (1998) 72–77.
[20] S.-P. Naik, A.-S. Chiang, R.-W. Thompson, F.-C. Huang, Formation of silicalite-1 hollow spheres by the self-assembly of nanocrystals, Chem. Mater. 15 (2003) 787–792.
[21] E.A. Lalla, S. Shkolyar, C.M. Gilmour, A. D, M. Konstantinidis, Lozano-Gorrín, J. Freemantle, M.G. Daly, Structural and vibrational analyses of $CePO_4$ synthetic monazite samples under an optimized precipitation process, J. Mol. Struct. 1223 (2021), 129150.
[22] A.-M. Seydoux-Guillaume, R. Wirth, L. Nasdala, M. Gottschalk, J.-M. Montel, W. Heinrich, An XRD, TEM and Raman study of experimentally annealed natural monazite, Phys. Chem. Miner. 29 (2002) 240–253.
[23] L. Cai, J. He, Q. Liu, T. Yao, L. Chen, W. Yan, F. Hu, Y. Jiang, Y. Zhao, T. Hu, Y. Jiang, Y. Zhao, T. Hu, Z. Sun, S. Wei, Vacancy-induced ferromagnetism of MoS_2 nanosheets, J. Am. Chem. Soc. 137 (2015) 2622–2627.
[24] G. Liu, A.W. Robertson, M.J. Li, W. Kuo, M.T. Darby, M.H. Muhieddine, Y.C. Lin, K. Suenaga, M. Stamatakis, J.H. Warner, S.E. Tsang, MoS_2 monolayer catalyst doped with isolated Co atoms for the hydrodeoxygenation reaction, Nat. Chem. 9 (2017) 810–816.
[25] F. Bai, L. Xu, X. Zhai, X. Chen, W. Yang, Vacancy in ultrathin 2D nanomaterials toward sustainable energy application, Adv. Energy Mater. 10 (2020), 1902107.
[26] R. Kahlaoui, K.I. Sobrados, R. Jimenez, J. Sanz, R. Ternane, Cation miscibility and lithium mobility in nasicon $Li_{1+x}Ti_{2-x}Sc_x(PO_4)_3$ ($0 \leq x \leq 0.5$) series: a combined NMR and impedance study, Inorg. Chem. 56 (2017) 1216–1224.
[27] G. Gouget, M. Pellerin, R. Orabi, L. P. D'Alençon, T. Mercier, C. B. Murray, Rare-earth sulfide nanocrystals from wet colloidal synthesis: tunable compositions, size-dependent light absorption, and sensitized rare-earth luminescence, J. Am. Chem. Soc. 143 (2021), 3300-3305.
[28] X. Yu, B. Kim, Y.K. Kim, Highly enhanced photoactivity of anatase TiO_2 nanocrystals by controlled hydrogenation-induced surface defects, ACS Catal. 3 (2013) 2479–2486.
[29] Y. Chen, J. Mandal, W. Li, A. S.-W, C.C. Tsai, Colored and paintable bilayer coatings with high solar-infrared reflectance for efficient cooling, Sci. Adv. 17 (2020) 6.
[30] J.F. Hoffmann, A.H. Roos, F. Schmitt, D. Hinderberger, W.H. Binder, Fluorescent and water dispersible single–chain nanoparticles: core–shell structured compartmentation, Angew. Chem. 133 (2021) 7899–7906.
[31] C. Dejoie, P. Martinetto, E. Dooryhee, P. Strobel, S. Blanc, P. Bordat, R. Brown, F. Porcher, M.S. Rio, M. Anne, Indigo@Silicalite: a new organic−inorganic hybrid pigment, ACS Appl. Mater. Interfaces 2 (2010) 2308–2316.
[32] J.Y. Ding, Q.-S. Wu, Y. Li, Q. Long, Y. Wang, X. Ma, Y. Wang, Self-activated yellow light emitting phosphors of α, β–$Ca_3B_2N_4$ with long afterglow properties, Inorg. Chem. 21 (2016) 10990–10998.
[33] M.H. Park, J. Park, J. Lee, H.S. So, H. Kim, S.-H. Jeong, T.H. Han, C. Wolf, H. Lee, S. Yoo, T.W. Lee, Efficient perovskite light-emitting diodes using polycrystalline core–shell-mimicked nanograins, Adv. Funct. Mater. (2019), 1902017.